

Article

Open Access



Li₂SO₄ coating for enhanced electrochemical performance of Co-free, Li-rich layered oxide cathode

Jung Hyeon Moon¹, Hyeonmuk Kang¹, GyuSeong Hwang¹, Junho Lee¹, GeunHyeong Shin², Gyungtae Kim³, Heechan Kang¹, EunAe Cho^{1,*}

¹Department of Materials Science and Engineering, Korea Advanced Institute of Science and Technology (KAIST), Daejeon 34141, Republic of Korea.

²Division of Future Vehicles, Korea Advanced Institute of Science & Technology (KAIST), Daejeon 34141, Republic of Korea.

³Department of Measurement & Analysis, National NanoFab Center (NNFC), Daejeon 34141, Republic of Korea.

*Correspondence to: Prof. EunAe Cho, Department of Materials Science and Engineering, Korea Advanced Institute of Science and Technology (KAIST), 291 Daehak-ro, Yuseong-gu, Daejeon 34141, Republic of Korea. E-mail: eacho@kaist.ac.kr

How to cite this article: Moon, J. H.; Kang, H.; Hwang, G.; Lee, J.; Shin, G.; Kim, G.; Kang, H.; Cho, E. Li₂SO₄ coating for enhanced electrochemical performance of Co-free, Li-rich layered oxide cathode. *Energy Mater.* **2025**, *5*, 500110. <https://dx.doi.org/10.20517/energymater.2025.36>

Received: 6 Mar 2025 **First Decision:** 19 Mar 2025 **Revised:** 8 Apr 2025 **Accepted:** 18 Apr 2025 **Published:** 19 May 2025

Academic Editor: Wei Tang **Copy Editor:** Ping Zhang **Production Editor:** Ping Zhang

Abstract

In the continued evolution toward high-performance lithium (Li)-ion batteries, cobalt (Co) has presented itself as a major obstacle due to its price, toxicity and supply. Thus, Co-free, Li-rich layered oxide cathodes (CF-LLC) have garnered interest for their exclusion of cobalt and high theoretical capacity. Nevertheless, CF-LLC suffers from issues such as sluggish kinetics, voltage fade and low early capacity due to the increase in cation mixing resulting from the absence of cation-ordering cobalt. To mitigate this, a sulfate coating was applied to the cathode carbonate precursor prior to lithiation, resulting in the formation of a Li₂SO₄-coated CF-LLC. The Li₂SO₄ coating prevents the agglomeration of primary particles during lithiation, thereby reducing the primary particle sizes. As a result, Li diffusion pathways are shortened, enhancing Li diffusivity. The coating also prevents transition metal dissolution by acting as a protective barrier against electrolytic reactions. With the Li₂SO₄ coating, first cycle capacity increased from 205.1 mAh g⁻¹ to 259.0 mAh g⁻¹, and first cycle Coulombic efficiency also increased from 76.6% to 83.6%. Moreover, after 100 cycles, the Li₂SO₄-coated sample showed a good 84.7% capacity retention and an improved average voltage fade per cycle of 2.79 mV.

Keywords: Co-Free Li-rich layered oxide, Li₂SO₄, Li diffusivity, particle size, structural degradation



© The Author(s) 2025. **Open Access** This article is licensed under a Creative Commons Attribution 4.0 International License (<https://creativecommons.org/licenses/by/4.0/>), which permits unrestricted use, sharing, adaptation, distribution and reproduction in any medium or format, for any purpose, even commercially, as long as you give appropriate credit to the original author(s) and the source, provide a link to the Creative Commons license, and indicate if changes were made.



INTRODUCTION

Over the past decades, lithium-ion batteries (LIB) have become a primary focus of research in the field of secondary batteries due to their applicability especially in the electric vehicle (EV) market. In this market, specific attention has been placed into increasing the energy density of LIBs in order to increase the driving range^[1-3]. Li-rich layered oxide cathodes (LLCs) are one of the candidates as a high-performance LIB cathode material due to their high practical specific capacity ($\sim 250 \text{ mAh}\cdot\text{g}^{-1}$) and high operating midpoint voltage (MPV) ($\sim 3.6 \text{ V}$)^[4]. Consequently, LLCs exhibit some of the highest energy density in layered oxide cathode materials. This can be explained by the structure of LLCs, where there are excess lithium ions in the transition metal (TM) layer, allowing the theoretical capacity to be greater than that of conventional layered oxide cathodes^[5].

Due to the rising price of Co and controversy surrounding its toxicity and supply, recent efforts have focused on excluding Co from the typical nickel-cobalt-manganese (NCM) TM blend to produce Co-free, layered oxide cathodes^[6-8]. Such trends have crossed over to the field of LLC research, making Co-free LLCs (CF-LLCs) also a new research topic of interest^[9]. CF-LLCs offer cheaper yet easier-to-produce batteries without sacrificing theoretical capacity.

However, previous research has shown that the CF-LLCs also suffer from the typical issues that plague LLCs, such as rapid structural degradation. Upon performing charge/discharge cycles, the layered oxide phase shifts to a less ordered spinel structure, and then to a rocksalt structure in its finality^[10]. As a result, the mid-point discharge voltage decays, leading to a loss in specific energy. Moreover, Co offers the highest electrical conductivity among the TMs, and acts as a structure stabilizer in the TM blend, reducing cation disordering^[11]. Due to the exclusion of Co, CF-LLCs exhibit reduced electrical conductivity and lower Li diffusivity^[12], leading to significantly worse early cycle capacity compared to conventional LLCs.

Attempts have been made to alleviate these issues through various cathode modification techniques. In particular, LLCs have been coated with oxides, fluorides, phosphates and conductive materials [Supplementary Table 1]^[13-20]. These coatings enhance the electrochemical performance of LLCs by inducing surface transformation to spinel phase, providing physical protection from electrolyte-induced degradation, modifying the cathode-electrolyte interphase (CEI) layer, and increasing ionic/electronic diffusivity. However, few studies have focused on the chemical protection of the LLC itself. On the other hand, dopants have also been used as a way to stabilize the structure during charge/discharge cycles through stabilization of the lattice oxygen, or as a way to improve the Li diffusion of the bulk material^[21,22]. While these modifications have successfully achieved their primary goals, they often fail to address both persistent issues of CF-LLC, structural degradation and low early capacity, leading to the modified materials that often perform worse than pristine LLCs.

In this study, we introduce a novel, dual-function coating strategy designed to simultaneously improve the early-cycle capacity of CF-LLCs and suppress undesired interfacial reactions with the electrolyte, as outlined in the schematic in Supplementary Figure 1. Lithium sulfate (Li_2SO_4) was selected as the coating material due to its ability not only to prevent primary particle agglomeration during annealing, but also to form in situ through a reaction of the sulfate precursor with Li species, resulting in a uniform and protective coating. Additionally, the use of nickel sulfate hexahydrate - a readily available and water-soluble TM salt - enables a simple, solution-based coating process, further enhancing the practicability and scalability of this approach.

The effects of Li_2SO_4 coating layers on the structural and interfacial properties of LLCs were thoroughly investigated before and after electrochemical cycling. To elucidate the morphological, compositional, and surface chemical changes, comprehensive characterization techniques were employed including scanning electron microscopy (SEM), energy-dispersive X-ray spectroscopy (EDS), high-angle annular dark-field scanning transmission electron microscopy (HAADF-STEM), X-ray photoelectron spectroscopy (XPS), attenuated total reflectance Fourier transform infrared spectroscopy (ATR-FTIR), X-ray diffraction (XRD), time-of-flight secondary ion mass spectrometry (TOF-SIMS) and Raman spectroscopy. In parallel, electrochemical analyses such as galvanostatic cycling, electrochemical impedance spectroscopy (EIS), differential capacity analysis (dQ/dV) and galvanostatic intermittent titration technique (GITT) were conducted to evaluate the functional role of the coating in enhancing Li^+ diffusion kinetics, interfacial stability, and overall electrochemical performance.

EXPERIMENTAL

Material synthesis

Synthesis of CF-LLC

CF-LLC was synthesized using a hydrothermal method. Stoichiometric amounts of manganese acetate tetrahydrate, $[\text{Mn}(\text{CH}_3\text{COO})_2 \cdot 4\text{H}_2\text{O}]$, Sigma Aldrich] and nickel Acetate tetrahydrate $[\text{Ni}(\text{OCOCH}_3)_2 \cdot 4\text{H}_2\text{O}]$, Sigma Aldrich] were added to a Teflon liner along with urea ($\text{CH}_4\text{N}_2\text{O}$, Junsei) and 50 mL solution mixture of deionized (DI) water and anhydrous ethyl alcohol ($\text{C}_2\text{H}_6\text{O}$, 99.9%, Samchun). The liner was placed in a stainless steel autoclave, sealed shut and heated in a convection oven to 200 °C for 12 h. The resulting mixture was then vacuum filtered with anhydrous ethyl alcohol ($\text{C}_2\text{H}_6\text{O}$, 99.9%, Samchun) and then dried overnight at 80 °C in a convection oven. The dried powder was then finely mixed in an agate mortar to produce the carbonate powder.

The carbonate was then mixed with stoichiometric amounts of lithium carbonate (Li_2CO_3 , Samchun) in an agate mortar and then pressed in a pellet mold. The resulting pellet was then placed in an alumina combustion boat and annealed in a tube furnace at 450 °C for 2 h and then at 900 °C for 12 h under constant airflow to produce CF-LLC.

Synthesis of Li_2SO_4 -coated CF-LLC

For the synthesis of Li_2SO_4 -coated CF-LLC (S-CF-LLC), DI water and the carbonate powder were mixed in a 2:1 wt ratio along with 6 wt% of nickel sulfate hexahydrate ($\text{NiSO}_4 \cdot 6\text{H}_2\text{O}$, Samchun) in a glass vial. After placing a magnetic stirring bar inside, the mixture was then placed on a stirrer/hotplate and dried overnight. The resulting coated carbonate mixture was then lithiated in the same process as above to produce S-CF-LLC.

The full synthesis schematic for CF-LLC and S-CF-LLC is outlined in [Supplementary Figure 2](#).

Material characterization

To examine the particle surface and primary particle size, SEM images were collected (SU5000, Hitachi). SEM-energy dispersive X-ray spectroscopy (SEM-EDS) data was collected in order to confirm the presence of the sulfate coating (Octane Elect EDS detector, EDAX). Primary particle size measurements were also performed to show the particle size distribution of each sample (ImageJ). Inductively coupled plasma optical emission spectroscopy was performed to examine the chemical composition of each sample (ICP-OES 720, Agilent). Structural characterization was performed by obtaining XRD patterns with a 2θ range of $10^\circ \sim 145^\circ$ and a step size of 0.01° (Ultima IV, Rigaku). Rietveld refinement was performed to compare the lattice parameters of the CF-LLC and S-CF-LLC (FullProf). The cathode and anode surfaces

were analyzed using XPS Data to examine changes in surface properties prior to and after cycling. (Scientific K-Alpha+ XPS system, ThermoFisher Scientific). The film samples were loaded onto carbon tape inside a vacuum transfer holder for measurement. Peak shift was calibrated using the C-C C1s peak set at 284.8 eV as the charge correction reference^[23]. XPS depth profile was also collected using the aforementioned system with 40 sec etching time intervals in order to confirm surface level coating. ATR-FTIR was performed to confirm the sulfur species of the coating material (Nicolet iS50, ThermoFisher Scientific). HAADF-STEM was performed for examination of the coating layer using scanning transmission electron microscopy-energy dispersive X-ray spectroscopy (STEM-EDS) (Titan³ G2 60-300, FEI). HAADF-STEM was also additionally performed to examine the structure of the cathode materials prior to and after cycling (Spectra Ultra S/TEM, ThermoFisher Scientific). The HAADF-STEM samples were prepared through Focused Ion Beam (FIB) milling to obtain appropriate TEM samples with a sample thickness of 100 nm (Helios G5, ThermoFisher Scientific). HAADF-STEM data filtering and fast Fourier transform (FFT) were performed for analysis (DigitalMicrograph, Gatan). Raman spectra were obtained with a 633 nm laser source within a Raman shift window of 200 cm⁻¹ to 900 cm⁻¹ to examine the bulk structure before and after cycling (LabRAM HR Evolution, Horiba). Raman spectra data was normalized after measurements for comparative analysis (Origin Pro). TOF-SIMS data was obtained to examine surface ions after cycling (TOF-SIMS5, ION-TOF GmbH).

Electrochemical measurements

To evaluate the electrochemical performance of CF-LLC and S-CF-LLC, the cathode active materials (CAM) were mixed with Super-P carbon black powder and polyvinylidene fluoride (PVDF) in an 8:1:1 weight ratio in an agate mortar. After thorough mixing, 800 μ L of N-Methyl-2-pyrrolidone (NMP, Sigma Aldrich) was added to form a slurry. This slurry mixture was placed on Al foil and then doctor bladed at approximately 200 μ m thickness and then dried overnight at 80 °C in a vacuum oven. The resulting cathode film was punched using a 10 mm film punch to form circular films. The circular films were then pressed using a flat mold at 3000 psi for 10 sec before being placed inside the glovebox for cell assembly. Coin cell 2032 was constructed using premade 2032 coin cell parts (bottom/top cap, gasket, spring, 1t spacer) with a lithium metal chip as the counter-electrode, 2 layers of polypropylene film as the separator and 200 μ L of 1M LiPF₆ ethylene carbonate:diethyl carbonate (EC:DEC) as the electrolyte.

The coin cells were tested in a WBCS3000S (WonATech) test system for galvanostatic cycling. The coin cells were put through charge/discharge cycles at a voltage range of 2.0~4.8 V at 0.1 C for the first cycle followed by subsequent cycles at various 0.2 C for 99 cycles for a total of 100 cycles. All cycles were performed in a LCH-11-2C (Jeiotech) temperature chamber with the temperature set to 25 °C. dQ/dV was carried out using the IVMAN differential analysis software (WonATech). GITT analysis was also performed at 10 min current pulses of 0.2 C current followed by 4hr rest cycles. EIS was performed using a VersaSTAT4 (AMETEK) with a voltage amplitude of 10 mV and a frequency range of 10⁶ Hz to 10⁻³ Hz. EIS fitting was performed using ZMAN (Zive Lab).

RESULTS AND DISCUSSION

Characterization of CF-LLC and S-CF-LLC

To synthesize a CF-LLC, a carbonate precursor was prepared and lithiated. For the S-CF-LLC, the prepared carbonate precursor was immersed in an aqueous nickel sulfate (NiSO₄) solution prior to lithiation [Supplementary Figure 2]. XRD patterns of the prepared samples [Figure 1A] reveal that both samples show a hexagonal α -NaFeO₂ structure with the *R*-3*m* space group, corresponding to CF-LLC with the Li_{1.2}Mn_{0.6}Ni_{0.2}O₂ stoichiometry. Additionally, both samples display the LLC characteristic superlattice peaks in the 20° to 25° range, associated with the monoclinic Li₂MnO₃ phase with the *C*2/*m* space group^[9]. The (003) peaks were observed at around 18.67° for both samples (inset in Figure 1A), with similar lattice

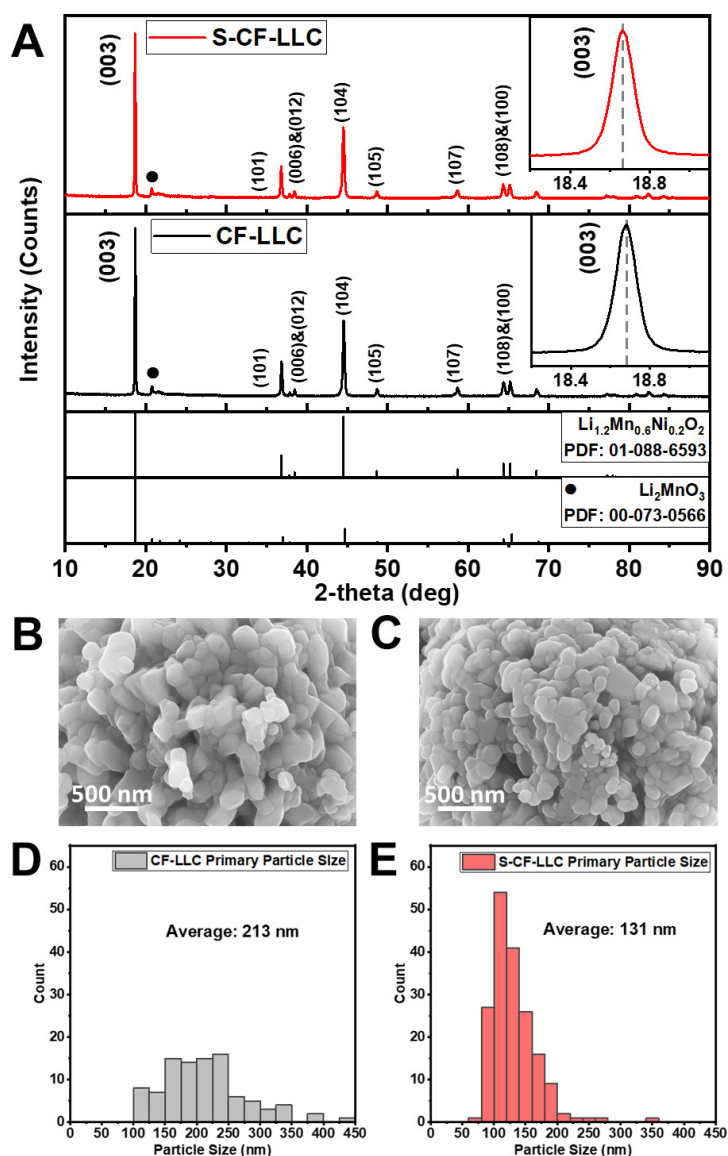


Figure 1. (A) XRD Patterns of CF-LLC and S-CF-LLC with (003) peak inset and corresponding PDF of $\text{Li}_{1.2}\text{Mn}_{0.6}\text{Ni}_{0.2}\text{O}_2$ and Li_2MnO_3 ; High-magnification SEM images of primary particles of (B) CF-LLC and (C) S-CF-LLC and the corresponding primary particle size distribution of (D) CF-LLC and (E) S-CF-LLC. XRD: X-ray diffraction; SEM: scanning electron microscopy; CF-LLC: Co-free, Li-rich layered oxide cathodes; S-CF-LLC: Li_2SO_4 -coated CF-LLC.

parameters [Supplementary Table 2] determined through XRD refinement. The peak intensity ratio between the (003) and (104) peaks [Supplementary Figure 3A] was approximately 1.7 for both samples, indicating formation of a well-ordered structure^[24]. Furthermore, the well-split peak pairs of (006)&(012) and (108)&(100) [Supplementary Figure 3B] confirm the high crystallinity of both samples^[25]. These results demonstrate that the prepared samples possess a well-defined CF-LLC structure corresponding to $\text{Li}_{1.2}\text{Mn}_{0.6}\text{Ni}_{0.2}\text{O}_2$ stoichiometry, and that the sulfate coating has negligible effects on their crystal structure^[26].

SEM images [Supplementary Figure 4A and B] show that both samples consist of spherical secondary particles with diameters of approximately 3~4 μm , though larger secondary particles have been observed up to 10 μm . Notably, S-CF-LLC exhibits smaller primary particles [Figure 1B and C] with an average particle

size of 131 nm, compared to 213 nm for C-F-LLC [Figure 1D and E]. These results suggest that the sulfate coating effectively suppressed the agglomeration of primary particles during the lithiation process. Seeing as most of the primary particles in S-CF-LLC fall in the range of 100~150 nm, smaller than the 150~250 nm range observed for CF-LLC, the coating likely formed at the primary particle level, thereby significantly reducing their size.

EDS mapping images [Figure 2A and B] display a uniform distribution of TMs (Mn, Ni) in both samples. Notably, S-CF-LLC reveals distinct sulfur (S) signals, while CF-LLC exhibits S signals indistinguishable from the background. The EDS spectrum [Supplementary Figure 5A and B] confirms the presence of S K α 1 peak only in S-CF-LLC. CF-LLC comprises 0.0 atm% S, 0.6 atm% Ni, 3.0 atm% Mn and 33.3 atm% O, while S-CF-LLC contains 0.1 atm% S, 1.2 atm% Ni, 3.8 atm% Mn and 40.8 atm% O [Supplementary Table 3]. As SEM-EDS does not give us accurate chemical stoichiometries, chemical compositions were also determined using ICP-OES, assuming stoichiometry for Li and O as 1.2 due to the difficulty in accurately measuring these elements with ICP-OES^[27]. Sulfur was omitted from ICP-OES measurements due to challenges such as low sensitivity, spectral interferences and volatility in the plasma^[28]. As shown in Supplementary Table 4, both samples show chemical compositions closely aligned with the stoichiometry of Li_{1.2}Mn_{0.6}Ni_{0.2}O₂.

To further investigate the chemical state and distribution of sulfur in S-CF-LLC, S 2p XPS spectra were collected and compared with CF-LLC [Figure 2C]. S-CF-LLC displays a clear peak at binding energy of around 169.5 eV, corresponding to lithium sulfate (Li₂SO₄)^[29], which is not observed in CF-LLC. In accordance with this, Li 1s XPS spectra [Figure 2D] of S-CF-LLC also show a peak at binding energy of around 55.8 eV, corresponding to Li₂SO₄^[30], which is not present in CF-LLC. Furthermore, the XPS S 2p depth profile with 40 sec etching time intervals [Supplementary Figure 6] demonstrates that the sulfate peak intensity decreases with increasing etching time, indicating that sulfate exists only as a surface coating layer and not within the bulk. Additionally, ATR-FTIR spectra [Supplementary Figure 7] show a distinct peak in the asymmetric S-O stretching mode region for S-CF-LLC, which is absent in CF-LLC, confirming the presence of a sulfate in S-CF-LLC^[31].

As discussed above, the smaller primary particle sizes of S-CF-LLC suggest that the sulfate exerts its effects at the primary particle level. To corroborate this, a FIB-milled S-CF-LLC sample was prepared for HAADF-STEM imaging [Figure 3A]. EDS mapping of S-CF-LLC primary particles reveals Mn and Ni are uniformly distributed throughout the primary particles, while S signals are more prominently detected along the grain boundaries of the primary particle. An EDS line profile shows the S signal intensity peak across the grain boundaries of the primary particles [Figure 3B]. EDS area profiles [Figure 3C] confirm higher S K intensity in regions covering the grain boundaries, compared to the centers of the primary particle. These results indicate that the primary particles of S-CF-LLC are successfully coated with a Li₂SO₄ coating layer.

Electrochemical performance

Figure 4 shows the comprehensive electrochemical performance of CF-LLC, and S-CF-LLC. In the first cycle [Figure 4A], CF-LLC exhibits a reduced specific discharge capacity (SC) of 205.1 mAh·g⁻¹ and a Coulombic efficiency (CE) of 76.6%, attributed to the exclusion of Co, which results in lowered kinetics such as reduced electronic conductivity and a higher degree of disordering^[11,12]. In contrast, S-CF-LLC outperforms CF-LLC, delivering a SC of 259.0 mAh·g⁻¹ and a CE of 83.6%. The superior performance of S-CF-LLC can be attributed to two key factors: the smaller primary particles [Figure 1B and C] and the pre-formed Li₂SO₄ coating layer [Figures 2 and 3]. The smaller particle size shortens the Li diffusion pathway, lowering overpotential and increasing SC, while the Li₂SO₄ coating layer mitigates surface

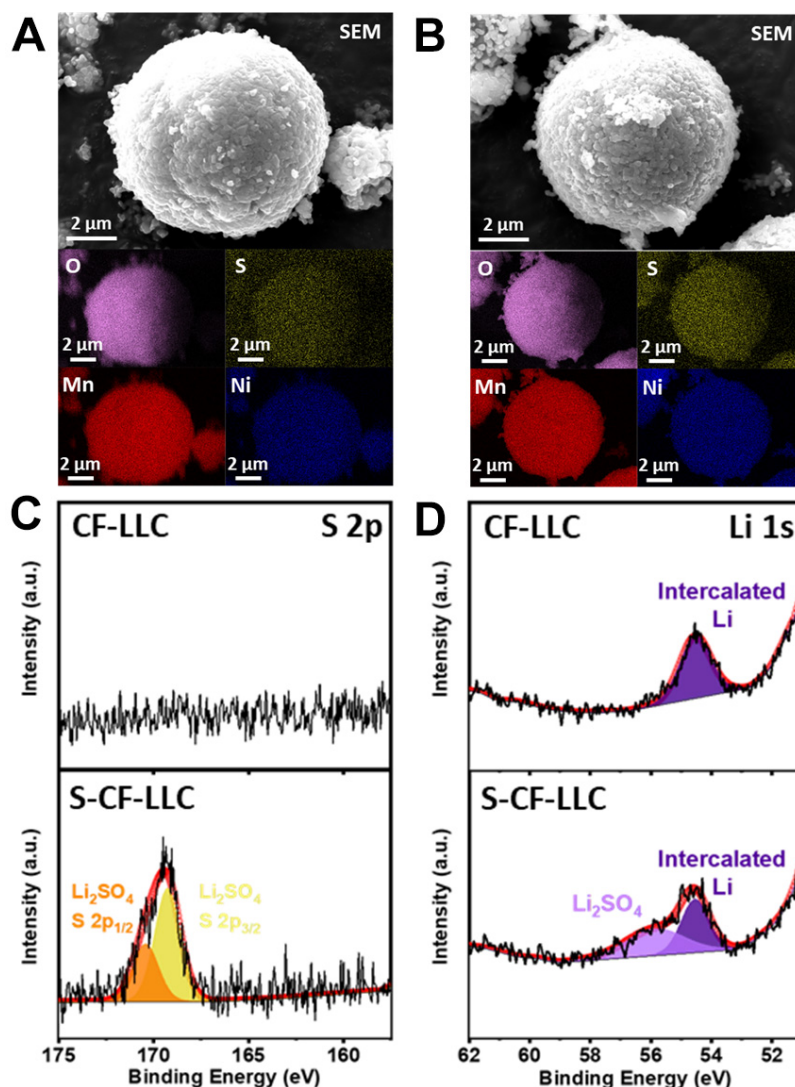


Figure 2. SEM-EDS images of (A) CF-LLC and (B) S-CF-LLC and their corresponding EDS mapping images; (C) XPS S 2p surface spectra of CF-LLC and S-CF-LLC; (D) XPS Li 1s surface spectra of CF-LLC and S-CF-LLC. SEM-EDS: Scanning electron microscopy-energy dispersive X-ray spectroscopy; CF-LLC: Co-free, Li-rich layered oxide cathodes; XPS: X-ray photoelectron spectroscopy; S-CF-LLC: Li_2SO_4 -coated CF-LLC.

reactions, reducing Li consumption and thereby enhancing CE^[32,33].

Figure 4B and C shows the SC and CE over 100 cycles for CF-LLC and S-CF-LLC. After 100 cycles, CF-LLC exhibits a relatively low specific discharge capacities of $175.2 \text{ mAh}\cdot\text{g}^{-1}$, corresponding to capacity retention of 96.0% (calculated from the second cycle), respectively. In contrast, S-CF-LLC maintains a high SC of $210.5 \text{ mAh}\cdot\text{g}^{-1}$ whilst maintaining a good 84.7% capacity retention. The high capacity retention of CF-LLC can be attributed to the sluggish kinetics, which results in a partially realized first cycle oxygen plateau and suppression of TM migration^[34]. Moreover, the lower charge capacity indicates that CF-LLC hardly undergoes deep delithiation due to its sluggish kinetics. As a result, CF-LLC experiences reduced volume change and thus, is less susceptible to capacity decaying issues such as cracking and the formation of stacking faults^[35]. However, this capacity retention comes at the expense of SC, which hinders the viability of CF-LLC as a high energy density cathode material. In contrast, S-CF-LLC offers a more favorable balance

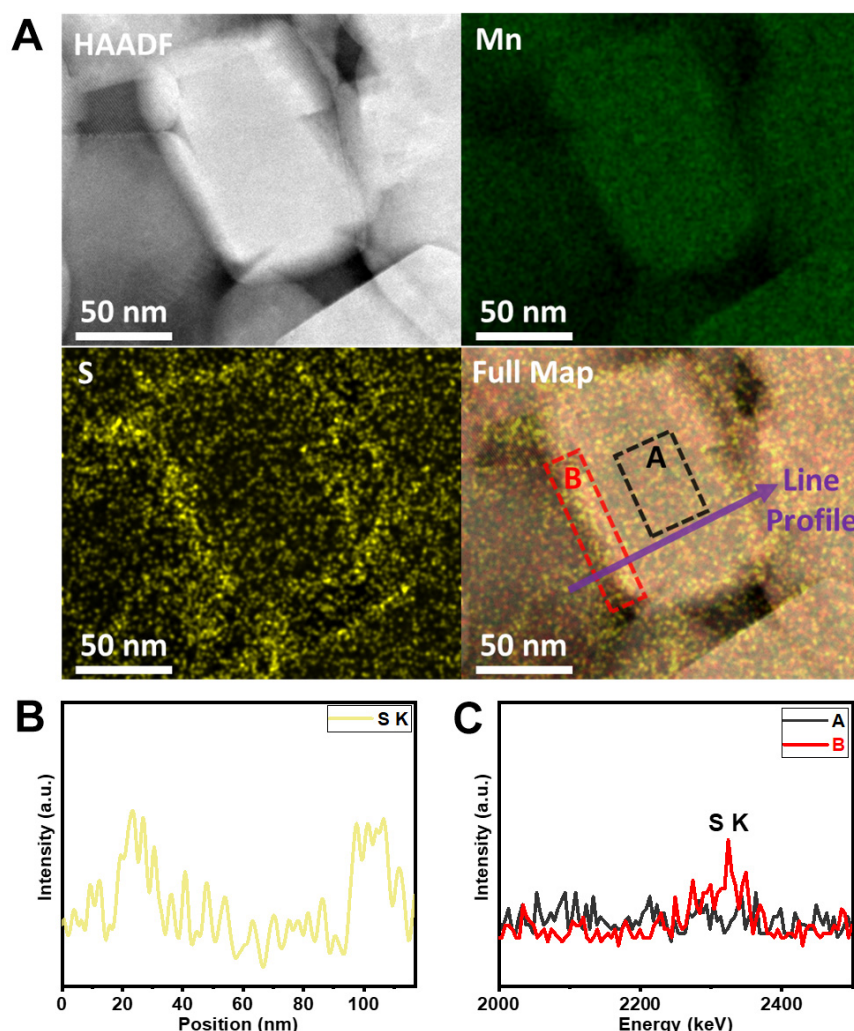


Figure 3. (A) HAADF-STEM images of a S-CF-LLC primary particle and the corresponding STEM-EDS mapping images; (B) Line profile EDS and (C) Area profile EDS of the S-CF-LLC primary particle. HAADF-STEM: High-angle annular dark-field scanning transmission electron microscopy; SEM-EDS: scanning electron microscopy-energy dispersive X-ray spectroscopy; S-CF-LLC: Li_2SO_4 -coated CF-LLC.

between high SC and good capacity retention, making it a more promising candidate for practical applications.

Both CF-LLC and S-CF-LLC also exhibited a high average CE of > 99% (calculated from the second cycle) over 100 cycles with S-CF-LLC showing a slight improvement of 99.2% over 99.1% of CF-LLC, indicating better reversibility of the Li^+ intercalation/de-intercalation process.

Voltage fade results from both bulk structural degradation and surface degradation. Oxygen release at the surface during the first cycle can induce TM migration, which can contribute to voltage decay^[4,36]. Moreover, uncoated cathode surfaces are susceptible to hydrogen fluoride (HF) etching, leading to TM dissolution and formation of unstable, thick CEI layers, that can increase overpotential and thus, lower the discharge voltage^[37,38]. Therefore, to evaluate voltage fade^[36] and examine the extent of material degradation, midpoint discharge voltage (MPV) was recorded from the charge-discharge curves over 100 cycles [Figure 4D]. The average change in voltage per cycle (ΔV) was 2.79 mV for S-CF-LLC, which is markedly

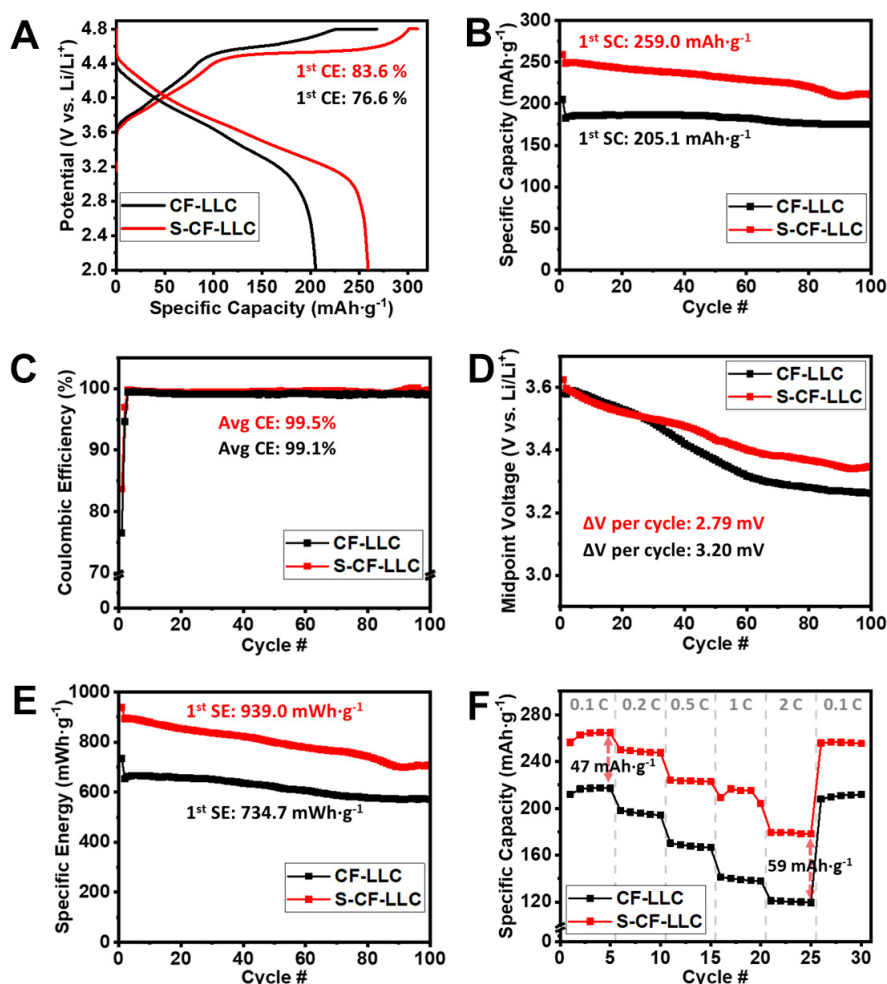


Figure 4. Electrochemical performance charts of LLC, CF-LLC and S-CF-LLC: (A) 1st cycle charge-discharge curves; (B) specific discharge capacity across 100 cycles; (C) Coulombic efficiency across 100 cycles; (D) midpoint voltage across 100 cycles; (E) specific discharge energy across 100 cycles; (F) Rate capability test of CF-LLC and S-CF-LLC. C-rate was increased sequentially from 0.1, 0.2, 0.5, 1, 2 C with 5 cycles per C-rate, after which the C-rate was returned to 0.1 C. CF-LLC: Co-free, Li-rich layered oxide cathodes; S-CF-LLC: Li_2SO_4 -coated CF-LLC.

lower than 3.20 mV for CF-LLC, suggesting reduced structural degradation.

Moreover, while smaller particle sizes typically increase surface area and exacerbate voltage fade^[39], S-CF-LLC outperforms CF-LLC in voltage fade due to the protective Li_2SO_4 coating, which counteracts the effects of reduced particle size. The reduction in structural degradation will be examined in detail in later sections through various analytical techniques.

Increasing energy density is one of the key goals in the development of next-generation LIBs. The specific discharge energy density (SE), calculated as the product of SC and MPV^[40] (Figure 4E), was 939.0 $\text{mWh}\cdot\text{g}^{-1}$ for S-CF-LLC for the first cycle, significantly higher than that of CF-LLC (734.7 $\text{mWh}\cdot\text{g}^{-1}$) and remained high after 100 cycles at 704.5 $\text{mWh}\cdot\text{g}^{-1}$ compared to 571.5 $\text{mWh}\cdot\text{g}^{-1}$ of CF-LLC.

Finally, rate capability of CF-LLC and S-CF-LLC was evaluated through five charge-discharge cycles at various C-rates (0.1 C, 0.2 C, 0.5 C, 1 C and 2 C in order and then returning to 0.1 C, Figure 4F). S-CF-LLC

consistently shows increased SC compared to CF-LLC across all C-rates, with the capacity difference increasing from 47.4 mAh·g⁻¹ at 0.1 C to 58.9 mAh·g⁻¹ at 2 C. Extended cycling at high C-rates of 1C and 3C [Supplementary Figure 8A and B] further confirms the superior rate performance of S-CF-LLC, compared to CF-LLC. At 1 C, S-CF-LLC shows an impressive 2nd cycle capacity of 193.4 mAh·g⁻¹ compared to 136.5 mAh·g⁻¹ of CF-LLC, and a 190th cycle capacity retention of 80.8% compared to 73.6% of CF-LLC. Moreover, at 3 C, S-CF-LLC shows a high 2nd cycle capacity of 160.5 mAh·g⁻¹ compared to 98.4 mAh·g⁻¹ of CF-LLC.

Primary particle size reduction effect on electrochemical performance

In many previous studies, reducing primary particle size has been touted as an effective method to improve cathode material kinetics and electrochemical performance^[39,41,42]. To thoroughly investigate and validate this effect for S-CF-LLC, GITT was performed to compare the Li⁺ diffusivity of S-CF-LLC and CF-LLC with current pulses of 10 min and rest steps of 4 h during both charging and discharging [Supplementary Figure 9]. The Li⁺ diffusion coefficient (D_{Li^+}) was then calculated using an equation derived from Fick's 2nd law of diffusion along with potential changes calculated for each titration step as outlined in Supplementary Figure 10^[43]. As shown in Supplementary Figure 11A and B, near the end of the charge/discharge process, S-CF-LLC shows a higher D_{Li^+} value compared to CF-LLC. The reason for this behavior can be explained by the particle size reduction. At high states of charge, shrinkage of the pathway reduces the diffusivity [Supplementary Figure 11A]^[44]. However, the shortening of the channels through primary particle size reduction means that it is easier for Li⁺ in the bulk to be diffused out. Similarly, at low states of charge during the discharging process, Li⁺ diffusivity decreases due to the decrease in Li⁺ vacancy [Supplementary Figure 11B]^[45]. Shortened Li⁺ pathways mean that even with lowered Li⁺ vacancies, it is easier for the Li⁺ to diffuse into the cathode, given that the enlarged surface area can also accommodate increased interfacial reactions.

Li⁺ diffusivity was also calculated using EIS to further verify the above findings. Supplementary Figure 12A shows the Nyquist plots of CF-LLC and S-CF-LLC prior to cycling. It can be seen that both samples show similar charge transfer resistance and ohmic resistance, with the only difference seen in the Warburg impedance. The Warburg impedance can then be plotted against the reciprocal of the square root of the angular frequency to obtain the slope which is the Warburg factor^[46]. This plot is illustrated in Supplementary Figure 12B, which shows that the Warburg factor for S-CF-LLC is lower than that of CF-LLC (306.6 and 730.2 Ω·s^{1/2}, respectively). Since the Warburg factor is a denominator in the D_{Li^+} equation and the rest of the factors are assumed constants for both samples, it can be said that S-CF-LLC has a higher D_{Li^+} value than CF-LLC, which is in accordance with GITT results^[46]. Thus, the increase in Li⁺ diffusivity through primary particle size reduction can be seen as a major factor in the improvement of electrochemical performance.

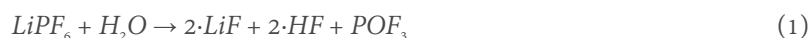
Another commonly used electrochemical analytical technique to examine capacity is dQ/dV which can give insight on the voltage windows where the capacity originates from, and the corresponding redox reactions that are often assigned to these voltage windows. Supplementary Figure 13 shows the dQ/dV plot of CF-LLC and S-CF-LLC for both charge/discharge at the 10th cycle, which clearly outlines the origin of the capacity difference between the two samples. Though S-CF-LLC shows general increase in dQ/dV across the entire potential range, the largest differences lay in the lower potential windows for both charging and discharging steps (3~3.5 V and 2.6~3.2 V, respectively). The low potential region has been attributed to Mn⁴⁺/Mn³⁺ redox and anionic redox in previously published literature, and has often been cited as exhibiting sluggish kinetics compared to the rapid Ni^{4+/3+/2+} redox activity^[47]. In the case of S-CF-LLC, particle size reduction has been demonstrated, through GITT and EIS data, to effectively enhance kinetics. As a result, the observed capacity increase can be partially attributed to the improved kinetics enabling

greater Mn^{4+/3+} activity, as well as a higher degree of anionic redox, which is made possible after a longer oxygen evolution plateau in the first cycle relative to CF-LLC. The influence of particle size on the dQ/dV difference is further supported by the absence of any significant increase in dQ/dV intensity for S-CF-LLC compared to CF-LLC in the higher potential region (3.5~4 V). Moreover, it is likely that a greater portion of Mn dissolves out from CF-LLC during cycling or become electrochemically inactive TM oxides, further reducing its contribution to overall capacity, compared to S-CF-LLC.

Li₂SO₄ coating effect and surface degradation analyses

Outside of primary particle size reduction, the other purpose of the dual-effect coating procedure is to create a protective Li₂SO₄ coating layer at a primary particle level. As surface area increases with the reduction of primary particle size, it is important that surface stability is increased to offset the increase in potential unwanted surface reactions. As Li₂SO₄ coating layer has been characterized to be successfully synthesized, samples of CF-LLC and S-CF-LLC cathode films prior to and after 100 cycles were prepared for comparison to examine the efficacy of the Li₂SO₄ coating layer.

XPS analysis of the cathode film prior to and after 100 cycles is illustrated in Figure 5. F 1s spectra of CF-LLC and S-CF-LLC [Figure 5A and B] both appear very similar prior to cycling, with a main PVDF peak at around 687.8 eV (as PVDF is used as the film binder) and a small LiF peak at around 684.8 eV that is the result of small amounts of LiF formation from PVDF during the cathode film synthesis process^[48,49]. However, F 1s spectra of the samples develop a large deviation in regards to the aforementioned LiF peak after 100 cycles. The peak appears much larger in relation to the main PVDF peak for CF-LLC compared to the Li₂SO₄-coated S-CF-LLC. The proposed reasoning is twofold: LiF formation due to electrolyte decomposition and LiF and MF₂ formation due to HF attack. Firstly, the LiPF₆ salt contained in the electrolyte can decompose, forming small amounts of LiF on the surface of the cathode^[50]. However, this is not expected to be the dominant LiF-forming reaction. Secondly, and more importantly, the LiPF₆ salt, when reacting with small amounts of water, can produce HF through^[51]:



The HF product can then react with the cathode surface in:



This not only causes the dissolution of TMs (through MF₂ formation) causing structural degradation loss in electrochemical performance, but also produces additional water, which can restart the reaction cycle^[37,52]. The result is that LiF and MF₂ (which have similar binding energy levels) progressively form more and more on the cathode surface whilst reducing performance, causing the LiF/MF₂ peak to grow. In contrast to the bare CF-LLC surface, the Li₂SO₄ coating on the surface of S-CF-LLC can react with HF in:



In contrast to CF-LLC, although this reaction does produce LiF (as seen by the small growth in LiF peak), it does not produce any water, ending the reaction cycle. Thus, due to the chemically protective Li₂SO₄ coating, S-CF-LLC undergoes less TM dissolution as evidenced by the F 1s spectra. This can be further corroborated by Supplementary Figure 14A and B, which shows reduced Mn³⁺ and Mn²⁺ peak growth after 100 cycles for the Mn 2p spectra for S-CF-LLC compared to CF-LLC, showing that the oxidation state of Mn species at the surface is higher due to less surface reactions^[53]. Supplementary Figure 14C also shows the

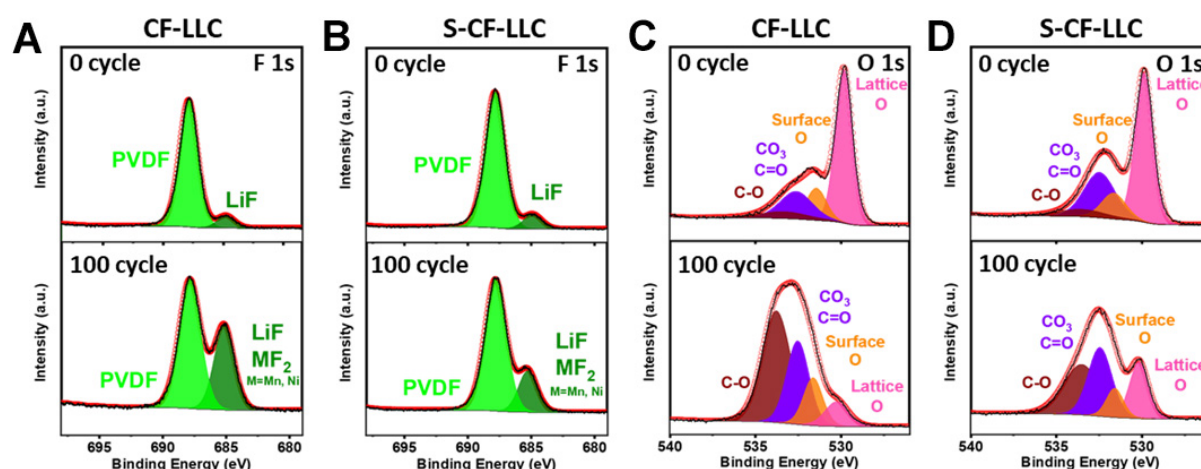


Figure 5. XPS analysis of (A) CF-LLC F 1s spectra before and after 100 cycles; (B) S-CF-LLC F 1s spectra before and after 100 cycles; (C) CF-LLC O 1s spectra before and after 100 cycles; (D) S-CF-LLC O 1s spectra before and after 100 cycles. XPS: X-ray photoelectron spectroscopy; CF-LLC: Co-free, Li-rich layered oxide cathodes; S-CF-LLC: Li_2SO_4 -coated CF-LLC.

presence of Li_2SO_4 for S-CF-LLC after cycling, indicating that the protective coating is durable. In addition, [Supplementary Figure 15A–D](#) shows the Mn 2p and Ni 2p spectra of the lithium metal anode and the PP separator extracted from both CF-LLC and S-CF-LLC half-cells. It has been reported that TMs deposit onto the anode after dissolution^[54]. Thus, examining the lithium metal anode and the separator (which are deposited with Li dendrites) can show us the amount of TMs that have dissolved and been deposited on to the lithium metal. Overall, the anode and separator used in S-CF-LLC half cells show much lower Ni 2p and Mn 2p signals compared to CF-LLC, indicating that less TM dissolution has occurred due to the protective Li_2SO_4 coating layer.

O 1s spectra of CF-LLC and S-CF-LLC [Figure 5C and D] also show the effect of the Li_2SO_4 coating on the surface prior to and after cycling. Prior to cycling, O 1s spectra of both samples show a large main peak that corresponds to the lattice oxygen peak (~ 530.0 eV). Beyond this main peak, there is a peak attributed to surface oxygen species (~ 531.8 eV) and $\text{CO}_3/\text{C}=\text{O}$ and C-O peaks (~ 532.5 eV and ~ 533.6 eV, respectively) that are attributed to cathode residual/CEI species^[55]. After 100 cycles, S-CF-LLC shows the enlargement of these surface/CEI species peaks relative to the lattice oxygen peak due to the formation of CEI layers upon cycling. However, this enlargement is much smaller in scale compared to that seen in the CF-LLC spectra after 100 cycles. It has been reported in other works that charging/discharging to high potential can cause instability of the CEI layer and continued formation of CEI species^[37]. However, coating layers have been found to mitigate this continued CEI formation, resulting in a lower amount of CEI species detected in the O 1s spectra as seen in the S-CF-LLC spectra^[56]. This reduction in CEI species formation from Li_2SO_4 coating also means reduced electrolyte consumption from decomposition reactions and reduced overall overpotential.

To validate the proposed chemically protective mechanism of Li_2SO_4 , TOF-SIMS analysis was conducted on CF-LLC and S-CF-LLC cathode films before and after 100 charge-discharge cycles. As seen in the surface mass spectra [Figure 6A], whereas no distinct HSO_4^- peaks around 96.96 m/z were observed in either sample prior to cycling, a prominent HSO_4^- peak emerges in the S-CF-LLC sample after 100 cycles. These results indicate that the chemical reaction between Li_2SO_4 and HF occurred to some extent, supporting the chemically protective mechanism of Li_2SO_4 coating layers^[57]. Furthermore, the TOF-SIMS 3D mapping [Figure 6B] reveals a uniform distribution of HSO_4^- in the S-CF-LLC sample after cycling, whereas the other

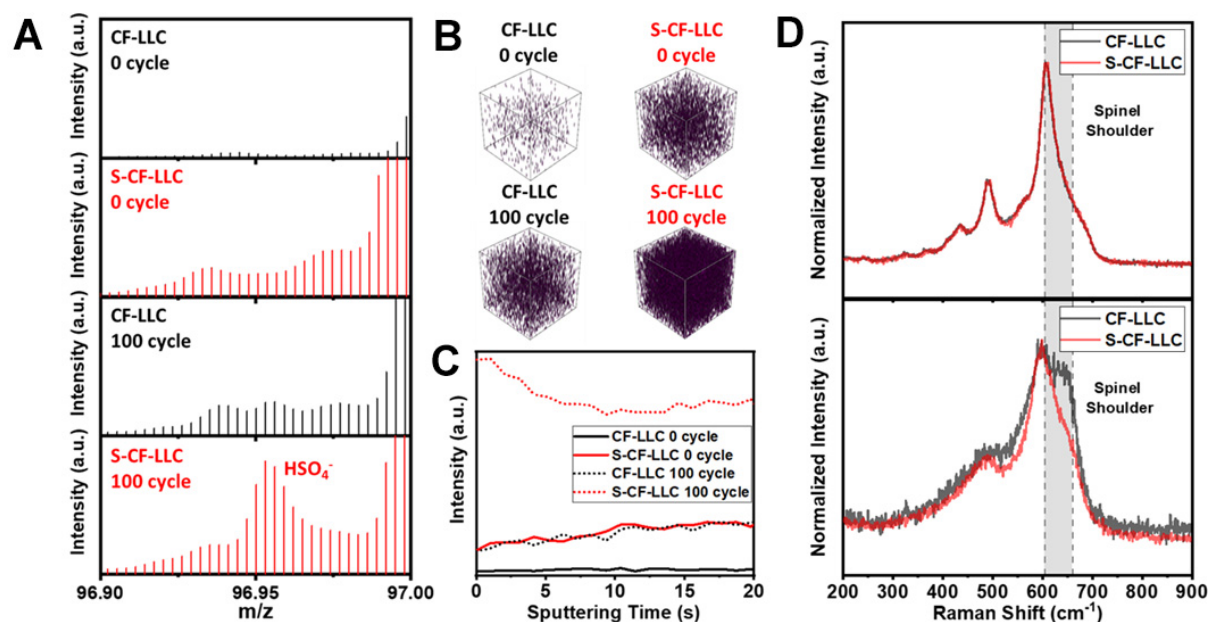


Figure 6. (A) TOF-SIMS data for CF-LLC and S-CF-LLC prior to and after 100 cycles and the corresponding (B) TOF-SIMS 3D mapping and (C) TOF-SIMS depth profile; (D) Raman spectra for CF-LLC and S-CF-LLC prior to and after 100 cycles. TOF-SIMS: Time-of-flight secondary ion mass spectrometry; CF-LLC: Co-free, Li-rich layered oxide cathodes; S-CF-LLC: Li₂SO₄-coated CF-LLC.

samples show only background level signals with no significant intensity at similar m/z values. This is corroborated by the TOF-SIMS depth profile [Figure 6C], where the HSO₄⁻ signal intensity in S-CF-LLC is significantly higher than in any other samples, with its peak concentration localized near the surface. These results collectively confirm the chemically protective role of Li₂SO₄ during cycling.

Raman spectra of CF-LLC and S-CF-LLC were analyzed to examine the structural degradation that may have occurred due to surface TM dissolution. As shown in Figure 6D, both samples show completely overlapping Raman spectra prior to cycling, with LiMO₂ peaks at 608 and 492 cm⁻¹ and the Li₂MnO₃ peak at 435 cm⁻¹ which are characteristic of LLC materials^[24]. However, after cycling, CF-LLC Raman spectra show a clear growth of a spinel phase shoulder peak around 605~660 cm⁻¹^[24]. This is evidence of structural degradation due to TM dissolution during cycling.

In order to physically observe the worsened structural degradation during cycling, HAADF-STEM images of CF-LLC and S-CF-LLC samples were taken prior to and after 100 cycles. Prior to cycling, both CF-LLC and S-CF-LLC samples exhibit a well-defined layered structure with a similar interlayer spacing of approximately 0.48 nm [Supplementary Figure 16A and B]. In contrast, post-cycling observations reveal structural changes in the surface regions of both samples [Figure 7A and B], while the layered structure in the bulk remains largely preserved. To investigate these structures' degradation in more detail, FFT was applied to the high-resolution STEM images [Figure 7C and D]. Specifically, the surface region of CF-LLC, approximately 10 nm thick, was found to consist of two distinct sublayers: an inner disordered (disordered layered) region and an outer rock salt phase. The disordered layered phase retains some characteristics of the original layered structure but displays additional bright atoms between the TM layers, indicative of TM migration into the Li layers. This transformation is reflected in the FFT patterns by the relative dimming of the (003) and (101) spots, compared to (006) spots^[58], which is characteristic of the disordered layered phase, an intermediate structure phase between the layered and rock salt phase^[58]. The outermost rock salt phase is clearly distinguishable in both the STEM and FFT images, showing an increased density of bright

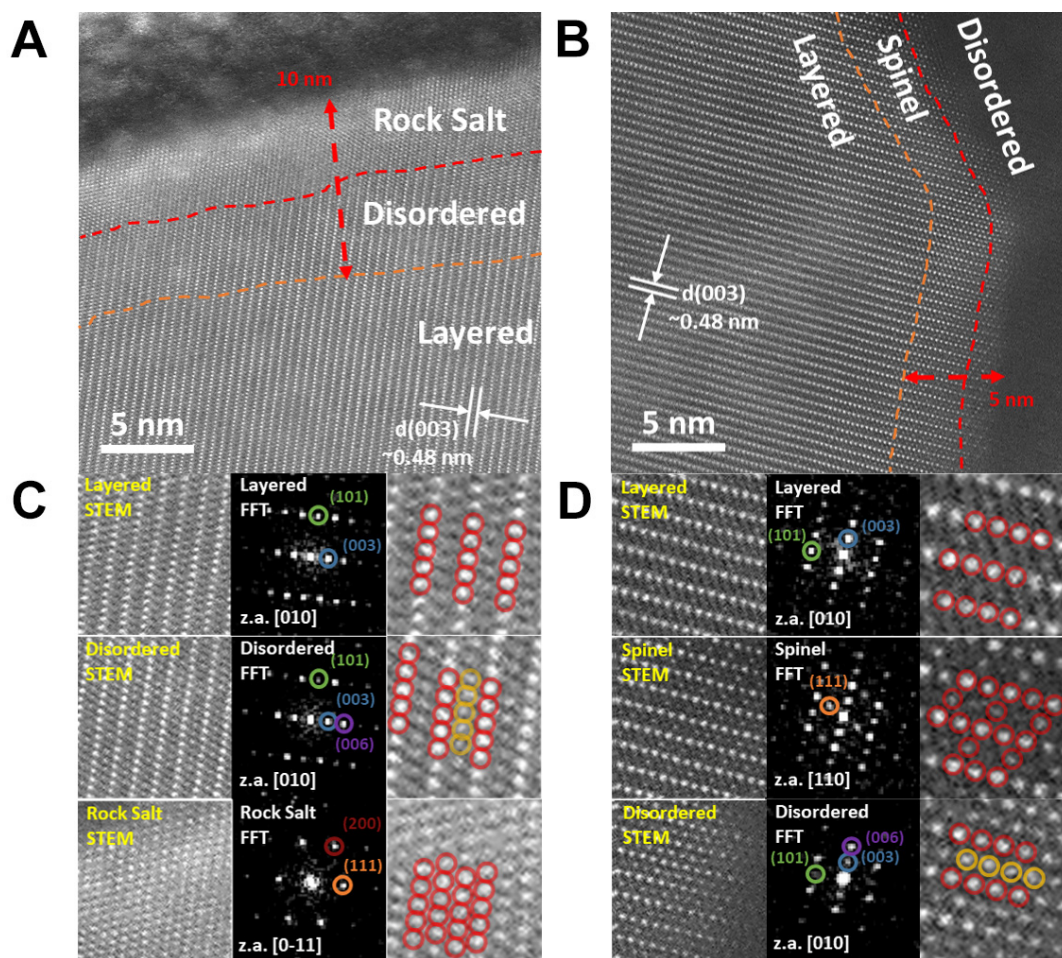


Figure 7. HAADF-STEM images of (A) CF-LLC and (B) S-CF-LLC after 100 cycles and the corresponding magnified images/FFT of each phase for (C) CF-LLC and (D) S-CF-LLC. HAADF-STEM: High-angle annular dark-field scanning transmission electron microscopy; CF-LLC: Co-free, Li-rich layered oxide cathodes; S-CF-LLC: Li_2SO_4 -coated CF-LLC.

TM atoms and forming a well-defined strip characteristic of rock salt phase. In contrast, S-CF-LLC [Figure 7B and D] shows a surface region, approximately 5 nm thick, consisting of an inner spinel layer and an outer disordered layer. The spinel layer displays several distinguishable features. Firstly, STEM images reveal regularly spaced TM atoms within the Li layer, which is characteristic of a Fd-3m spinel phase^[59]. Moreover, FFT images display new inter-layer spots, which are also characteristic of the Fd-3m spinel phase^[59], which has been reported to be electrochemically active. Therefore, this observation not only support our findings on the protective nature of Li_2SO_4 coating, but also demonstrates the dual-functionality of the coating: it suppresses the formation of the electrochemically inactive rock salt phase and facilitate the formation of an intermediate, electrochemically active spinel phase, thereby enhancing electrochemical performance. These findings are in accordance with earlier XPS and Raman results, both of which indicate reduced surface degradation in S-CF-LLC due to Li_2SO_4 coating. Furthermore, dQ/dV analysis also suggested the electrochemical participation of a spinel phase.

Finally, EIS results show a similar difference in surface degradation with CF-LLC and S-CF-LLC after cycling as presented Supplementary Figure 17A. EIS fitting was performed with the equivalent circuit illustrated in Supplementary Figure 17B, and the resulting film resistance (R_f) and charge transfer resistance (R_{ct}) are presented in Supplementary Table 5. Most notably, R_{ct} of CF-LLC was calculated to be 1,840.0 Ω ,

which is a large increase from the R_{ct} of S-CF-LLC of 818.8 Ω . R_{ct} is influenced largely by electronic conductivity of the cathode material, which is in turn affected by Ni content, as Ni inherently has a higher electronic conductivity than Mn^[11]. The increased dissolution of Ni as presented in the XPS data is likely the cause of the reduced electronic conductivity and increased R_{ct} of CF-LLC, which has been partially mitigated by the Li_2SO_4 coating for S-CF-LLC^[60,61].

CONCLUSION

In this study, a dual-effect sulfate coating method was explored to improve the electrochemical performance of a CF-LLC. Coating the carbonate precursor material prior to the annealing process produced a cathode material with a Li_2SO_4 coating layer at the primary particle level that both protects the cathode material and also prevents agglomeration during the annealing process. The prevention of agglomeration resulted in the reduction of cathode primary particle size, improving its kinetics and Li^+ diffusivity which were initially sluggish due to the exclusion of Co. Furthermore, the protective Li_2SO_4 coating layer serves as a chemically protective layer, preventing the continued decomposition of the electrolyte and more importantly, preventing HF attack and in turn, reducing TM dissolution from the surface. Through these modifications, S-CF-LLC exhibited a significantly improved 1st cycle SC of 259.0 $\text{mAh}\cdot\text{g}^{-1}$ and 1st cycle CE of 83.6% compared to both CF-LLC and even Co-inclusive LLC. Beyond the first cycle, S-CF-LLC also demonstrated a good capacity retention of 84.7% after 100 cycles, as well as improved voltage fade, specific discharge energy and rate capability compared to the pristine cathode. In all, this simple and scalable dual-effect coating method potentially opens up the commercial viability and applicability of CF-LLCs that have previously been inadequate due to low electrochemical performance.

DECLARATIONS

Acknowledgments

The authors would like to thank the KAIST Analysis Center for Research Advancement (KARA), and the National NanoFab Center for granting access to their equipment.

Authors' contributions

First author of this study and led the conceptualization, design, experimental processes, data analyses, data interpretation, data presentation and manuscript writing: Moon, J. H.

Made contributions to conceptualization, data analyses and data interpretation: Kang, H.; Hwang, G.; Lee, J.; Shin, G.

Made significant contributions to formal analysis: Kim, G.

Made contributions to data interpretation and manuscript draft: Kang, H.

Corresponding author of this study and provided administrative, technical, and material support as well as contributing to conceptualization, data analyses and data interpretation: Cho, E.

Availability of data and materials

The data supporting this article have been included as part of the [Supplementary Materials](#).

Financial support and sponsorship

This work was supported by the National Research Foundation of Korea (NRF) grant funded by the Korean government (MSIT) (RS-2023-00247245), and by the Korea Institute for Advancement of Technology (KIAT) grant funded by the Korean government (MOTIE) (P0017120, Competency Development Program for Industry Specialists).

Conflicts of interest

All authors declared that there are no conflicts of interest.

Ethical approval and consent to participate

Not applicable.

Consent for publication

Not applicable.

Copyright

© The Author(s) 2025.

REFERENCES

- Mohammadi, F.; Saif, M. A comprehensive overview of electric vehicle batteries market. *e-Prime. Adv. Electr. Eng. Electron. Energy*. **2023**, 3, 100127. DOI
- Rangarajan, S. S.; Sundararaj, S. P.; Sudhakar, A. V. V.; et al. Lithium-ion batteries-the crux of electric vehicles with opportunities and challenges. *Clean. Technol.* **2022**, 4, 908-30. DOI
- Sankaran, G.; Venkatesan, S. An overview of lithium-ion batteries for electric mobility and energy storage applications. *IOP. Conf. Ser. Earth. Environ. Sci.* **2022**, 1042, 012012. DOI
- Xie, Y.; Jin, Y.; Xiang, L. Li-rich layered oxides: structure, capacity and voltage fading mechanisms and solving strategies. *Particuology* **2022**, 61, 1-10. DOI
- Yan, J.; Liu, X.; Li, B. Recent progress in Li-rich layered oxides as cathode materials for Li-ion batteries. *RSC. Adv.* **2014**, 4, 63268-84. DOI
- Banza, L. N. C.; Casas, L.; Haufroid, V.; et al. Sustainability of artisanal mining of cobalt in DR congo. *Nat. Sustain.* **2018**, 1, 495-504. DOI PubMed PMC
- Campbell, G. A. The cobalt market revisited. *Miner. Econ.* **2020**, 33, 21-8. DOI
- Sun, Y. K.; Lee, D. J.; Lee, Y. J.; Chen, Z.; Myung, S. T. Cobalt-free nickel rich layered oxide cathodes for lithium-ion batteries. *ACS. Appl. Mater. Interfaces.* **2013**, 5, 11434-40. DOI PubMed
- Ding, X.; Luo, D.; Cui, J.; Xie, H.; Ren, Q.; Lin, Z. An ultra-long-life lithium-rich $\text{Li}_{1.2}\text{Mn}_{0.6}\text{Ni}_{0.2}\text{O}_2$ cathode by three-in-one surface modification for lithium-ion batteries. *Angew. Chem. Int. Ed.* **2020**, 59, 7778-82. DOI
- Kim, S.; Cho, W.; Zhang, X.; Oshima, Y.; Choi, J. W. A stable lithium-rich surface structure for lithium-rich layered cathode materials. *Nat. Commun.* **2016**, 7, 13598. DOI PubMed PMC
- Manthiram, A. A reflection on lithium-ion battery cathode chemistry. *Nat. Commun.* **2020**, 11, 1550. DOI PubMed PMC
- Clément, R. J.; Lun, Z.; Ceder, G. Cation-disordered rocksalt transition metal oxides and oxyfluorides for high energy lithium-ion cathodes. *Energy. Environ. Sci.* **2020**, 13, 345-73. DOI
- Zhou, C.; Wang, P.; Zhang, B.; et al. Suppressing the voltage fading of $\text{Li}[\text{Li}_{0.2}\text{Ni}_{0.13}\text{Co}_{0.13}\text{Mn}_{0.54}]\text{O}_2$ cathode material via Al_2O_3 coating for Li-ion batteries. *J. Electrochem. Soc.* **2018**, 165, A1648. DOI
- Zhai, X.; Zhang, P.; Huang, H.; et al. Surface modification of Li-rich layered $\text{Li}_{1.2}\text{Mn}_{0.54}\text{Ni}_{0.13}\text{Co}_{0.13}\text{O}_2$ oxide with Fe_2O_3 as cathode material for Li-ion batteries. *Solid. State. Ionics.* **2021**, 366-7, 115661. DOI
- Lee, J.; Kang, H.; Moon, J.; et al. Enhancement of the cyclic stability of a Li-excess layered oxide through a simple electrode treatment for LiF-coating. *Electrochim. Acta.* **2025**, 524, 145919. DOI
- Zhao, T.; Chen, S.; Chen, R.; et al. The positive roles of integrated layered-spinel structures combined with nanocoating in low-cost Li-rich cathode $\text{Li}[\text{Li}_{0.2}\text{Fe}_{0.1}\text{Ni}_{0.15}\text{Mn}_{0.55}]\text{O}_2$ for lithium-ion batteries. *ACS. Appl. Mater. Interfaces.* **2014**, 6, 21711-20. DOI
- Wang, Y.; Yu, W.; Zhao, L.; et al. AlPO_4 - Li_3PO_4 dual shell for enhancing interfacial stability of Co-free Li-rich Mn-based cathode. *Electrochim. Acta.* **2023**, 462, 142664. DOI
- Sai, L.; Dai, Z.; Wang, Z.; Zhao, H.; Bai, Y. Multiple-functional $\text{LiTi}_2(\text{PO}_4)_3$ modification improving long-term performances of Li-rich Mn-based cathode material for advanced lithium-ion batteries. *J. Power. Sources.* **2024**, 613, 234870. DOI
- Wu, H.; Li, H.; Yang, P.; Xing, Y.; Zhang, S. Surface modification of $\text{Li}_{1.2}\text{Mn}_{0.6}\text{Ni}_{0.2}\text{O}_2$ with electronic conducting polypyrrole. *Int. J. Electrochem. Sci.* **2018**, 13, 6930-9. DOI
- Song, B.; Lai, M. O.; Liu, Z.; Liu, H.; Lu, L. Graphene-based surface modification on layered Li-rich cathode for high-performance Li-ion batteries. *J. Mater. Chem. A.* **2013**, 1, 9954-65. DOI
- Uzun, D. Boron-doped $\text{Li}_{1.2}\text{Mn}_{0.6}\text{Ni}_{0.2}\text{O}_2$ as a cathode active material for lithium ion battery. *Solid. State. Ionics.* **2015**, 281, 73-81. DOI
- Jiang, W.; Zhang, C.; Feng, Y.; et al. Achieving high structure and voltage stability in cobalt-free Li-rich layered oxide cathodes via selective dual-cation doping. *Energy. Storage. Mater.* **2020**, 32, 37-45. DOI
- Li, G.; You, L.; Wen, Y.; et al. Ultrathin Li-Si-O Coating layer to stabilize the surface structure and prolong the cycling life of single-

- crystal $\text{LiNi}_{0.6}\text{Co}_{0.2}\text{Mn}_{0.2}\text{O}_2$ cathode materials at 4.5 V. *ACS Appl. Mater. Interfaces*. **2021**, *13*, 10952-63. DOI
24. Celeste, A.; Tuccillo, M.; Santoni, A.; Reale, P.; Brutti, S.; Silvestri, L. Exploring a Co-free, Li-rich layered oxide with low content of nickel as a positive electrode for Li-ion battery. *ACS Appl. Energy Mater.* **2021**, *4*, 11290-7. DOI
25. Li, Y.; Bai, Y.; Wu, C.; et al. Three-dimensional fusiform hierarchical micro/nano $\text{Li}_{1.2}\text{Ni}_{0.2}\text{Mn}_{0.6}\text{O}_2$ with a preferred orientation (110) plane as a high energy cathode material for lithium-ion batteries. *J. Mater. Chem. A*. **2016**, *4*, 5942-51. DOI
26. Geng, F.; Wang, L.; Stralka, T.; et al. (111)-oriented growth and acceptor doping of transparent conductive CuI:S thin films by spin coating and radio frequency-sputtering. *Adv. Eng. Mater.* **2023**, *25*, 2201666. DOI
27. Kiciński, W.; Dyjak, S. Transition metal impurities in carbon-based materials: pitfalls, artifacts and deleterious effects. *Carbon* **2020**, *168*, 748-845. DOI
28. Martínez-sierra J, Galilea San Blas O, Marchante Gayón J, García Alonso J. sulfur analysis by inductively coupled plasma-mass spectrometry: a review. *Spectrochim. Acta. B*. **2015**, *108*, 35-52. DOI
29. Wahlqvist, M.; Shchukarev, A. XPS spectra and electronic structure of group IA sulfates. *J. Electron. Spectrosc. Relat. Phenom.* **2007**, *156-158*, 310-4. DOI
30. Liao, W.; Liu, H.; Qi, L.; et al. Lithium/bismuth co-functionalized phosphotungstic acid catalyst for promoting dinitrogen electroreduction with high Faradaic efficiency. *Cell. Rep. Phys. Sci.* **2021**, *2*, 100557. DOI
31. Lauer, A. R.; Hellmann, R.; Montes-Hernandez, G.; et al. Deciphering strontium sulfate precipitation via Ostwald's rule of stages: from prenucleation clusters to solution-mediated phase transformation. *J. Chem. Phys.* **2023**, *158*, 054501. DOI
32. Yoon, T.; Soon, J.; Lee, T. J.; Ryu, J. H.; Oh, S. M. Dissolution of cathode-electrolyte interphase deposited on $\text{LiNi}_{0.5}\text{Mn}_{1.5}\text{O}_4$ for lithium-ion batteries. *J. Power. Sources*. **2021**, *503*, 230051. DOI
33. Liao, J.; Zhang, Z.; Fan, W.; Wang, Q.; Liao, D. Synchronous construction of oxygen vacancies with suitable concentrations and carbon coating on the surface of Li-rich layered oxide cathode materials by spray drying for Li-ion batteries. *Electrochim. Acta*. **2022**, *405*, 139798. DOI
34. Gent, W. E.; Lim, K.; Liang, Y.; et al. Coupling between oxygen redox and cation migration explains unusual electrochemistry in lithium-rich layered oxides. *Nat. Commun.* **2017**, *8*, 2091. DOI
35. Singer, A.; Zhang, M.; Hy, S.; et al. Nucleation of dislocations and their dynamics in layered oxide cathode materials during battery charging. *Nat. Energy*. **2018**, *3*, 641-7. DOI
36. Abdel-ghany, A.; Hashem, A. M.; Mauger, A.; Julien, C. M. Lithium-rich cobalt-free manganese-based layered cathode materials for Li-ion batteries: suppressing the voltage fading. *Energies* **2020**, *13*, 3487. DOI
37. Hirooka, M.; Sekiya, T.; Omomo, Y.; et al. Degradation mechanism of LiCoO_2 under float charge conditions and high temperatures. *Electrochim. Acta*. **2019**, *320*, 134596. DOI
38. Zhuang, Z.; Wang, J.; Jia, K.; et al. Ultrahigh-voltage LiCoO_2 at 4.7 V by interface stabilization and band structure modification. *Adv. Mater.* **2023**, *35*, 2212059. DOI
39. Yabuuchi, N.; Kubota, K.; Aoki, Y.; Komaba, S. Understanding particle-size-dependent electrochemical properties of Li_2MnO_3 -based positive electrode materials for rechargeable lithium batteries. *J. Phys. Chem. C*. **2016**, *120*, 875-85. DOI
40. Li, Q.; Li, G.; Fu, C.; et al. Balancing stability and specific energy in Li-rich cathodes for lithium ion batteries: a case study of a novel Li-Mn-Ni-Co oxide. *J. Mater. Chem. A*. **2015**, *3*, 10592-602. DOI
41. Nitta, N.; Wu, F.; Lee, J. T.; Yushin, G. Li-ion battery materials: present and future. *Mater. Today*. **2015**, *18*, 252-64. DOI
42. Choi, H.; Schuer, A. R.; Moon, H.; Kuenzel, M.; Passerini, S. Investigating the particle size effect on the electrochemical performance and degradation of cobalt-free lithium-rich layered oxide $\text{Li}_{1.2}\text{Ni}_{0.2}\text{Mn}_{0.6}\text{O}_2$. *Electrochim. Acta*. **2022**, *430*, 141047. DOI
43. Gao, D.; Zeng, Z.; Mi, H.; et al. Enhanced structural stability and overall conductivity of Li-rich layered oxide materials achieved by a dual electron/lithium-conducting coating strategy for high-performance lithium-ion batteries. *J. Mater. Chem. A*. **2019**, *7*, 23964-72. DOI
44. McClelland, I.; Booth, S. G.; Anthonisamy, N. N.; et al. Direct observation of dynamic lithium diffusion behavior in nickel-rich, $\text{LiNi}_{0.8}\text{Mn}_{0.1}\text{Co}_{0.1}\text{O}_2$ (NMC811) cathodes using operando muon spectroscopy. *Chem. Mater.* **2023**, *35*, 4149-58. DOI
45. Zheng, J.; Shi, W.; Gu, M.; et al. Electrochemical kinetics and performance of layered composite cathode material $\text{Li}[\text{Li}_{0.2}\text{Ni}_{0.2}\text{Mn}_{0.6}]\text{O}_2$. *J. Electrochem. Soc.* **2013**, *160*, A2212. DOI
46. Chen, M.; Jiang, S.; Huang, C.; et al. Synergetic effects of multifunctional composites with more efficient polysulfide immobilization and ultrahigh sulfur content in lithium-sulfur batteries. *ACS Appl. Mater. Interfaces*. **2018**, *10*, 13562-72. DOI
47. Assat, G.; Foix, D.; Delacourt, C.; Iadecola, A.; Dedryvère, R.; Tarascon, J. M. Fundamental interplay between anionic/cationic redox governing the kinetics and thermodynamics of lithium-rich cathodes. *Nat. Commun.* **2017**, *8*, 2219. DOI PubMed PMC
48. Bag, S.; Zhou, C.; Kim, P. J.; Pol, V. G.; Thangadurai, V. LiF modified stable flexible PVDF-garnet hybrid electrolyte for high performance all-solid-state Li-S batteries. *Energy. Storage. Mater.* **2020**, *24*, 198-207. DOI
49. Khosla, N.; Narayan, J.; Narayan, R.; Sun, X.; Paranthaman, M. P. Nanosecond laser annealing of NMC 811 cathodes for enhanced performance. *J. Electrochem. Soc.* **2023**, *170*, 030520. DOI
50. Xu, J. Critical review on cathode-electrolyte interphase toward high-voltage cathodes for Li-ion batteries. *Nano-Micro. Lett.* **2022**, *14*, 166. DOI
51. Han, J. Y.; Jung, S. Thermal stability and the effect of water on hydrogen fluoride generation in lithium-ion battery electrolytes containing LiPF₆. *Batteries* **2022**, *8*, 61. DOI
52. Son, S.; Zhang, Z.; Gim, J.; et al. Transition metal dissolution in lithium-ion cells: a piece of the puzzle. *J. Phys. Chem. C*. **2023**, *127*,

- 1767-75. [DOI](#)
53. Zhang, W.; Sun, Y.; Deng, H.; et al. Dielectric polarization in inverse spinel-structured Mg_2TiO_4 coating to suppress oxygen evolution of Li-rich cathode materials. *Adv. Mater.* **2020**, *32*, 2000496. [DOI](#)
 54. Jung, R.; Linsenmann, F.; Thomas, R.; et al. Nickel, manganese, and cobalt dissolution from Ni-rich NMC and their effects on NMC622-graphite cells. *J. Electrochem. Soc.* **2019**, *166*, A378. [DOI](#)
 55. Björklund, E.; Brandell, D.; Hahlin, M.; Edström, K.; Younesi, R. How the negative electrode influences interfacial and electrochemical properties of $\text{LiNi}_{1/3}\text{Co}_{1/3}\text{Mn}_{1/3}\text{O}_2$ cathodes in Li-ion batteries. *J. Electrochem. Soc.* **2017**, *164*, A3054. [DOI](#)
 56. Gao, L.; Jin, X.; Li, Z.; Li, F.; Xu, B.; Wang, C. Ultrathin titanium dioxide coating enables high-rate and long-life lithium cobalt oxide. *Materials* **2024**, *17*, 3036. [DOI](#) [PubMed](#) [PMC](#)
 57. Holsclaw, C. M.; Sogi, K. M.; Gilmore, S. A.; et al. Structural characterization of a novel sulfated menaquinone produced by stf3 from mycobacterium tuberculosis. *ACS. Chem. Biol.* **2008**, *3*, 619-24. [DOI](#)
 58. Lin, Q.; Guan, W.; Meng, J.; et al. A new insight into continuous performance decay mechanism of Ni-rich layered oxide cathode for high energy lithium ion batteries. *Nano. Energy*. **2018**, *54*, 313-21. [DOI](#)
 59. Hua, W.; Chen, M.; Schwarz, B.; et al. Lithium/oxygen incorporation and microstructural evolution during synthesis of Li-rich layered $\text{Li}[\text{Li}_{0.2}\text{Ni}_{0.2}\text{Mn}_{0.6}]\text{O}_2$ oxides. *Adv. Energy. Mater.* **2019**, *9*, 1803094. [DOI](#)
 60. Choi, W.; Shin, H.; Kim, J. M.; Choi, J.; Yoon, W. Modeling and applications of electrochemical impedance spectroscopy (EIS) for lithium-ion batteries. *J. Electrochem. Sci. Technol.* **2020**, *11*, 1-13. [DOI](#)
 61. Lee, W.; Muhammad, S.; Kim, T.; et al. New insight into Ni-rich layered structure for next-generation Li rechargeable batteries. *Adv. Energy. Mater.* **2018**, *8*, 1701788. [DOI](#)